JGR Solid Earth

RESEARCH ARTICLE
10.1029/2018JB016964

Key Points:
- Thermal equation of state and single-crystal elasticity measurements is performed on omphacite crystals
- With the newly obtained thermoelastic parameters of omphacite, anisotropic seismic properties of eclogite are modeled
- The maximum *Vp*, *Vs*, and anisotropy contrast between pyrolite and eclogite is between 310 and 410 km

Supporting Information:
- Supporting Information S1

Correspondence to:
M. Hao and J. S. Zhang,
minghao@unm.edu;
jinzhang@unm.edu

Citation:
Hao, M., Zhang, J. S., Pierotti, C. E., Ren, Z., & Zhang, D. (2019). High-pressure single-crystal elasticity and thermal equation of state of omphacite and their implications for the seismic properties of eclogite in the Earth's interior. *Journal of Geophysical Research: Solid Earth*, *124*, 2368–2377. https://doi.org/10.1029/2018JB016964

Received 12 NOV 2018
Accepted 27 JAN 2019
Accepted article online 1 FEB 2019
Published online 2 MAR 2019

High-Pressure Single-Crystal Elasticity and Thermal Equation of State of Omphacite and Their Implications for the Seismic Properties of Eclogite in the Earth's Interior

Ming Hao[1], Jin S. Zhang[1,2], Caroline E. Pierotti[1,3], Zhiyuan Ren[1], and D. Zhang[4,5]

[1]Department of Earth and Planetary Sciences, University of New Mexico, Albuquerque, NM, USA, [2]Institute of Meteoritics, University of New Mexico, Albuquerque, NM, USA, [3]Albuquerque High School, Albuquerque, NM, USA, [4]Hawaii Institute of Geophysics and Planetology, University of Hawai'i at Mānoa, Honolulu, HI, USA, [5]GeoSoilEnviroCARS, University of Chicago, Argonne National Laboratory, Argonne, IL, USA

Abstract Omphacite is a major mineral phase of eclogite, which provides the main driving force for the slab subduction into the Earth's interior. We have measured the single-crystal elastic moduli of omphacite at high pressures for the first time up to 18 GPa at ambient temperature using Brillouin spectroscopy. A least squares fit of the velocity-pressure data to the third-order finite strain equation of state yields $K_{S0}' = 4.5$ (3), $G_0' = 1.6$ (1) with $\rho_0 = 3.34$ (1) g/cm^3, $K_{S0} = 123$ (3) GPa, and $G_0 = 74$ (2) GPa. In addition, the synchrotron single-crystal X-ray diffraction data have been collected up to 18 GPa and 700 K. The fitting to Holland-Powell thermal-pressure equation of state yields $K_{T0}' = 4.6$ (5) and $\alpha_0 = 2.7\,(8) \times 10^{-5}$ K^{-1}. Based on the obtained thermoelastic parameters of omphacite, the anisotropic seismic velocities of eclogite are modeled and compared with pyrolite between 200 and 500 km. The largest contrast between the eclogite and pyrolite in terms of seismic properties is observed between ~310 and 410 km.

1. Introduction

Omphacite is a clinopyroxene (Cpx) solid solution of Fe-bearing diopside ($CaMgSi_2O_6$) and jadeite ($NaAlSi_2O_6$) and is stable up to about 500-km depth in the Earth's interior (Irifune et al., 1986). It is also a major mineral component of eclogite (up to 75 vol%). Basalt, which makes up most of the Earth's oceanic crust, transforms into eclogite at the depth >~60 km (Ahrens & Schubert, 1975). Previous studies have suggested that eclogite remains denser than the surrounding mantle down to the base of the transition zone and therefore is considered one of the main driving forces for the slab subduction (Anderson, 2007; Moghadam et al., 2010; Peacock, 1996; Xu et al., 2008). Subducted eclogite is also an important source of the chemical heterogeneities in the Earth's mantle (Anderson, 2007; Kay & Kay, 1993; Moghadam et al., 2010; Peacock, 1996; Xu et al., 2008). Previous studies have proposed to utilize the unique seismic properties of eclogite to identify possible subduction channels and eclogite-rich regions in the Earth's interior (e.g., Ábalos et al., 2011; Mauler et al., 2000). Due to the elastically isotropic nature of garnet and the relatively small proportion (<10 vol%) of the silica minerals in eclogite (e.g., Aoki & Takahashi, 2004; Irifune et al., 2008; Liu et al., 2000; Sinogeikin & Bass, 2002), the seismic anisotropy of eclogite is primarily caused by the lattice preferred orientation of omphacite, including L type, S type, and SL type (e.g., J. Zhang et al., 2006; J. Zhang & Green, 2007). Thus, in order to model the seismic properties of eclogite in the Earth's interior, measurements of the density and single-crystal elastic properties of omphacite under relevant pressure (P)-temperature (T) conditions are needed.

Depending on the thermal history, natural omphacite crystals can display either a disordered C2/c or an ordered P2/n symmetry (Clark & Papike, 1968; Fleet et al., 1978). The P2/n and C2/c structures are similar, and the P2/n → C2/c phase transition at high T has no resolvable effect on the equation of state (EOS) of omphacite (Nishihara et al., 2003; Pandolfo et al., 2012a, 2012b). This study primarily focuses on the evolution of the elastic properties rather than the crystal structure of omphacite as a function of depth in the Earth's interior. Therefore, we do not differentiate the two structures of omphacite here.

Previous EOS studies on omphacite are mainly limited by the investigated P or T range or both (e.g., McCormick et al., 1989; Nishihara et al., 2003; Pandolfo et al., 2015, 2012a, 2012b; Pavese et al., 2000,

2001). For example, D. Zhang et al. (2016) performed single-crystal X-ray diffraction (XRD) experiments on omphacite up to 47 GPa at 300 K. Pandolfo et al. (2012b) measured the thermal expansion coefficients of omphacite up to 1073 K at 1 atm. The only available in situ high *P-T* EOS study for omphacite is performed on polycrystalline samples using multianvil press up to 10 GPa and thus is unable to cover the entire *P* stability field of omphacite in the Earth's interior (Nishihara et al., 2003). On the other hand, although the sound velocities of the Mg,Ca end member diopside have been studied at various *P-T* conditions (Isaak et al., 2006; Isaak & Ohno, 2003; Levien et al., 1979; Li & Neuville, 2010; Matsui & Busing, 1984; Sang et al., 2011; Sang & Bass, 2014; Walker, 2012), the single-crystal elastic properties of omphacite have only been measured at ambient condition (Bhagat et al., 1992) or investigated computationally at high-*P* 0-K conditions (Skelton & Walker, 2015). The lack of experimentally determined thermoelastic properties of omphacite, which is the most abundant mineral phase in eclogite, restricts our understanding of the subduction process as well as the possible seismic identification of eclogitic materials in the Earth's interior.

To fill in this knowledge gap, we performed high *P-T* single-crystal XRD measurements on natural P2/n omphacite crystals up to 18 GPa 700 K at GeoSoilEnviroCARS (GSECARS), Advanced Photon Source, Argonne National Laboratory, as well as single-crystal Brillouin spectroscopy measurements of the same crystals up to 18 GPa at 300 K at the high-*P* laser spectroscopy laboratory at University of New Mexico (UNM). The thermal EOS, single-crystal elastic moduli (C_{ij}), aggregate compressional (Vp) and shear (Vs) velocities, adiabatic bulk modulus (K_S), shear modulus (G), and their *P* dependences are determined and then utilized for calculating the seismic properties of eclogite in this study.

2. Experimental Methods

The P2/n omphacite crystals were hand-picked from a natural eclogite rock. The composition $Na_{0.289}Mg_{0.633}Ca_{0.68}Fe_{0.108}Al_{0.323}Si_{1.975}O_6$ was determined by electron probe microanalysis (EPMA), using the JEOL 8200 Electron Microprobe facility hosted by the Institute of Meteoritics at UNM. The JEOL 8200 Electron Microprobe is equipped with five wavelength dispersive X-ray spectrometers and an ultrathin-window energy dispersive X-ray spectrometer. The wavelength dispersive spectrometers are fitted with multiple analyzing crystals to provide quantitative analysis of all elements from Be to U. Selected crystals with ~1-mm size were used for EPMA analysis, operating at 15-kV accelerating voltage and 20-nA beam current. The beam spot size is smaller than 1 μm. The detailed analysis results can be found in Table S1 in the supporting information. Normalizing the chemical analysis in terms of diopside and jadeite yields a simplified composition of $Diopside_{70.5}Jadeite_{29.5}$. The crystals were then double-side polished into pellets with ~15-μm thickness. They were scratch free and inclusion free under optical examination. The polished samples were then cut into pieces with ~40-μm width for diamond anvil cell (DAC) loading.

Symmetric piston-cylinder DACs and BX90 DACs with standard 60° and 90° opening tungsten carbide backing seats were used for Brillouin and XRD measurements (Kantor et al., 2012). Re gaskets were preindented to 50- to 55-μm thickness with a pair of 350-μm culet diamonds, and 235- to 240-μm-diameter holes were drilled into the gaskets and served as sample chambers. Neon was gas loaded as the *P*-transmitting medium at GSECARS, Advanced Photon Source, Argonne National Laboratory (Rivers et al., 2008). For synchrotron high *P-T* XRD experiments, gold EOS was used for estimating the experimental *P*s. The *P* derivatives of the isothermal bulk modulus (K_{T0}') of gold vary from 5.0 to 6.2 in previous EOS studies (e.g., Anderson et al., 1989; Dorogokupets & Oganov, 2007; Fei et al., 2007, 2004; Greeff & Graf, 2004; Shim et al., 2002; Tsuchiya, 2003). At 18 GPa and 700 K, the maximum difference between the *P*s determined using different gold EOSs is ~0.3 GPa. In this study, we adopted the internally consistent thermal EOS of gold from Fei et al. (2007). For ambient-*T* high-*P* Brillouin spectroscopy experiments, two ruby spheres were loaded into each DAC and used as the *P* standard (Mao et al., 1978). The maximum *P* difference between the ruby spheres before and after the experiment is 0.2 GPa.

Ambient and high *P-T* single-crystal XRD experiments were carried out at GSECARS experimental station 13-BM-D and 13-BM-C. The X-ray opening angles for symmetric piston-cylinder DACs and BX90 DACs are ±14° and ±24°, respectively. At 13-BM-D, the X-ray is monochromated to 37.0 keV and focused to 6 μm × 15 μm. A stationary Perkin-Elmer image plate is used as a detector. Diffraction images were collected at 1° per step under step-scan mode, and the exposure time was 5 s per degree. At 13-BM-C, the X-ray beam

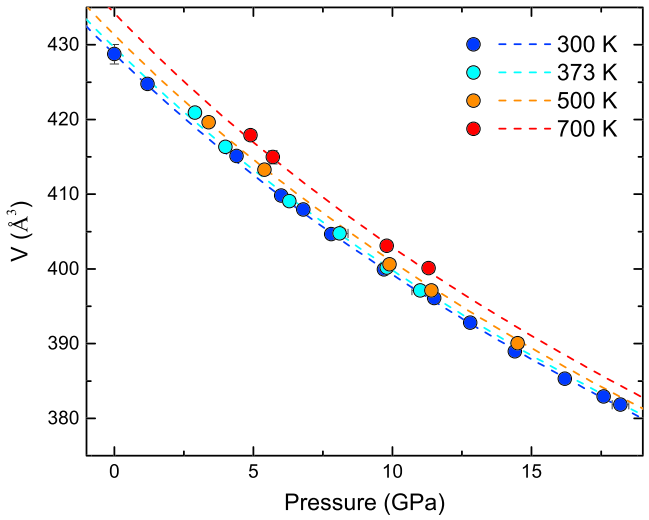

Figure 1. *P-V-T* data of omphacite with calculated isothermal compression curves.

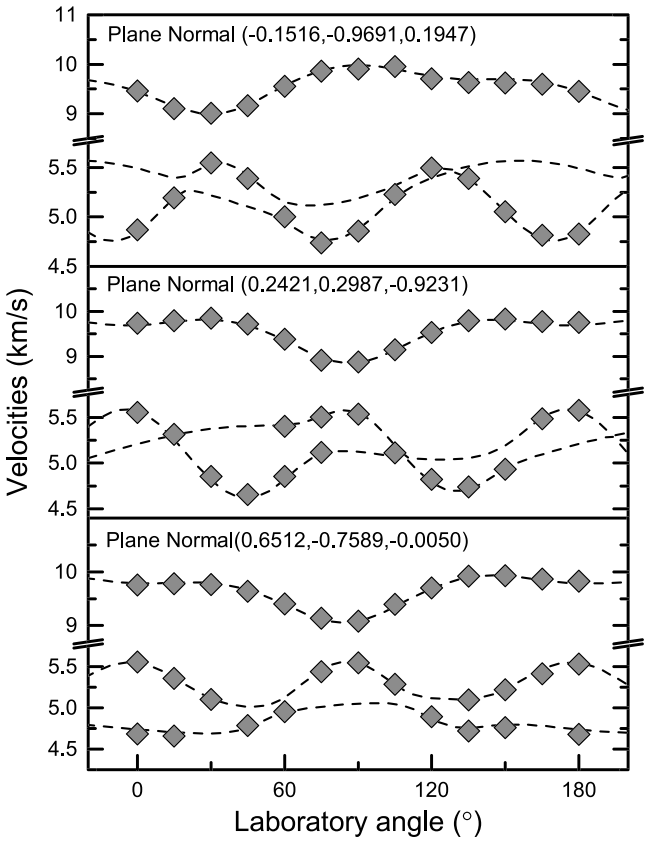

Figure 2. Measured acoustic velocities of omphacite as a function of laboratory *Chi* angles within the sample plane at 18 GPa. Dashed lines are the acoustic velocities calculated from the best fit single-crystal elasticity model; diamonds are the experimentally determined velocities. Errors are within the size of the symbols.

energy is 28.6 keV and the beam size is ~15 μm × 15 μm. The MAR165 Charge Coupled Device detector is placed on a rotational detector arm. Two different detector positions were used. One detector position was perpendicular to the incident X-ray beam, and the other detector position was rotated about the horizontal axis by 20° (D. Zhang et al., 2017). We collected both the wide-scan and 1° per step step-scan images with 3 s per degree exposure time. LaB6 powder was used to calibrate the detector geometry parameters in both stations.

For measurements at ambient condition, the polished plate-like crystals were oriented with their plane normals parallel to the incoming X-ray beam. The obtained ambient unit cell parameters were averaged from the three grains measured with different orientations: a = 9.584 (7) Å, b = 8.83 (2) Å, c = 5.2504 (4) Å, and β = 105.27(9)°. The calculated density ρ_0 is 3.34 (1) g/cm^3 at ambient condition. The face normals of the measured three samples are (−0.1516, −0.9691, 0.1947), (0.2421, 0.2987, −0.9231), and (0.6512, −0.759, −0.0050), close to (010), (001), and (1–10) directions. The angular uncertainties for the measured face normals are approximately 1–2° (Weidner & Carleton, 1977). For high *P-T* single-crystal XRD measurements, we used resistively heated DACs with Pt heaters to reach 373, 500, and 700 K at high-*P* conditions. The DACs were oriented in the way that the DAC axes were parallel to the incoming X-ray beam. The *T* was estimated from the two K-type thermal couples attached to the diamond anvils. The difference between the two *T* readings was smaller than 10 K.

The Brillouin spectroscopy experiments were performed at the high-*P* laser spectroscopy laboratory at UNM up to 18 GPa. A 300-mW 532-nm single-mode diode-pumped solid-state laser was used as a light source. The measurements were carried out using a 50° symmetric forward scattering geometry. The scattering angle was calibrated to be 50.37 (5)° using a standard silica glass Corning 7980 (J. S. Zhang et al., 2011, 2015). The pair of diamonds were oriented to ensure that the fast and slow directions matched each other. We used the three preoriented omphacite crystals measured at 13-BM-D for the Brillouin measurements at seven different *P*s. At each *P*, *Vp* and *Vs* were measured at 13 different *Chi* angles (0, 30, 60, 90, 120, 150, 180, 195, 225, 255, 285, 315, and 345) along the 360° azimuth to avoid any geometrical errors. All Brillouin spectra are with excellent signal-to-noise ratios. A typical Brillouin spectrum collected at 18 GPa is shown in Figure S1.

3. Results and Discussion

3.1. Thermal EOS of Omphacite

The single-crystal XRD images were analyzed using the ATREX IDL software package (Dera et al., 2013) to obtain the unit cell parameters (Table S2). Due to the use of crystals with different orientations in different experimental runs, we only performed thermal EOS fit to the unit cell volumes.

The ambient isothermal bulk modulus K_{T0} was calculated from the Reuss bond of the adiabatic bulk modulus $K_{S0}{}^{R}$ using equation (S1) (supporting information), and the value of 118.7 GPa was fixed in the thermal EOS fitting process. As pointed by Angel et al. (2018), the use of thermal Birch-Murnaghan EOS may suffer from the unphysical assumptions of constant $\partial K_T/\partial T$ and K_T' within the explored *P-T* range; thus, we chose to use the

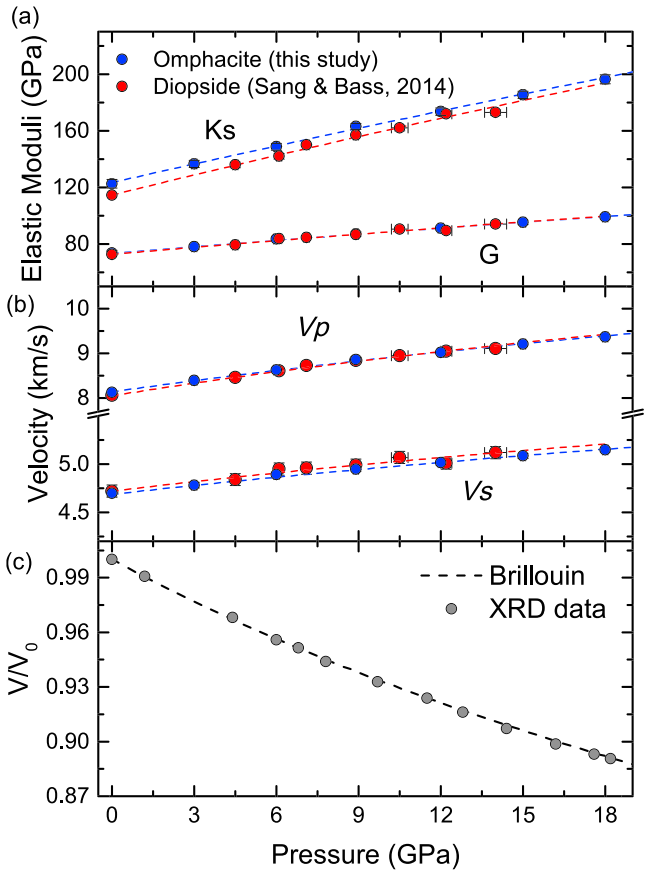

Figure 3. (a and b) The high-*P* K_S, *G*, *Vp*, and *Vs* of omphacite in this study are compared with the previous study of diopside (Sang & Bass, 2014). (c) The high-*P* normalized volumes V/V_0 calculated from the finite strain inversion of the sound velocity data are compared with direct measurements from X-ray diffraction (XRD) experiments.

Holland-Powell thermal-*P* EOS instead in this study (Holland & Powell, 2011; Birch, 1947; equation (S2)–(S4), supporting information). With fixed V_0 and K_{T0}, the fitting yields $K_{T0}' = 4.6$ (5) and $\alpha_0 = 2.7$ (8) $\times 10^{-5}$ K^{-1} (Figure 1). Our obtained K_{T0}' and α_0 values agree well with Pandolfo et al. (2012a, 2012b), D. Zhang et al. (2016), and Nishihara et al. (2003).

3.2. High-*P* Single-Crystal Elastic Properties of Omphacite

With known ρ_0 measured by single-crystal XRD, a least squares inversion of the Christoffel equation was used to calculate the best fit values for the 13 independent C_{ij}s of omphacite at ambient condition (Weidner & Carleton, 1977). The final results have a root-mean-square residual between the observed and modeled velocities of less than 50 m/s. The ambient aggregate elastic properties K_{S0} and G_0 were calculated using the Voigt-Reuss-Hill averaging scheme (Hill, 1963). As shown in Table S3, most C_{ij}s for the $Diopside_{70.5}Jadeite_{29.5}$ sample determined in this study are smaller than the values of a $Diopside_{34.1}Jadeite_{65.9}$ omphacite sample measured by Bhagat et al. (1992).

The high-*P* densities and single-crystal and aggregate elastic properties were calculated iteratively. Given an initial guess of the sample's high-*P* densities, a set of C_{ij}s, K_S, *G*, *Vp*, and *Vs* can be calculated by the least squares inversion of the Christoffel equation at each *P*. Note that the *Vp* and *Vs* are independent of the assumed density values, and thus, they represent the true aggregate *Vp* and *Vs* under high-*P* conditions. With fixed $\rho_0 = 3.34$ (1) g/cm^3, $K_{S0} = 123$ (3) GPa, and $G_0 = 74$ (2) GPa, we can then fit the obtained *P*-*Vp*-*Vs* data set to the third-order finite strain EOS (Davies, 1974; Davies & Dziewonski, 1975) and calculate the true high-*P* densities as well as the *P* derivatives of K_S and *G*. Finally, we recalculated the high-*P* single-crystal elasticity models with updated true densities. The calculated velocities from the final single-crystal C_{ij} model at 18 GPa are plotted with the measured velocities in Figure 2. The V/V_0 values calculated from the finite strain EOS also agree well with the XRD measurements (Figure 3c). All the C_{ij}s, K_S, *G*, *Vp*, *Vs*, and density values at different *P*s are listed in Table 1.

The aggregate elastic properties of omphacite are found to display a close-to-linear *P* dependence within the explored *P* range. K_{S0}' and G_0' are determined to be 4.5 (3) and 1.6 (1) with fixed $\rho_0 = 3.34$ (1) g/cm^3, $K_{S0} = 123$ (3) GPa, and $G_0 = 74$ (2) GPa. The K_{S0}' is indistinguishable from K_{T0}' considering their experimental uncertainties. Figures 3a and 3b show the K_S, *G*, *Vp*, and *Vs* of the omphacite in this study and the comparison with previous measurements of diopside (Sang & Bass, 2014). The K_{S0} and G_0 of jadeite (Kandelin & Weidner, 1988) are ~27% and ~19% higher than those of diopside, suggesting that the increase of jadeite component in Cpx stiffens the crystal structure and results in higher K_{S0} and G_0. However, the K_{S0}' and G_0' of diopside are slightly larger than omphacite. Thus, the K_S and *G* differences between diopside and omphacite decrease with *P* (Figure 3a). As a matter of fact, the shear moduli of omphacite and diopside are indistinguishable at *P* higher than 6 GPa. The *Vp* and *Vs* of diopside and omphacite are very similar over the entire *P* measurement range (<0.05 km/s difference, Figure 3b).

This study provides the first set of experimentally determined C_{ij}s of omphacite under high-*P* conditions (Table 1 and Figure 4). The dashed lines in Figure 4 are the finite strain fitting results of all C_{ij}s following the procedures listed in J. S. Zhang et al. (2018). Most of the C_{ij}s have close to linear *P* dependences up to 18 GPa, except C_{35} and C_{46}. Skelton and Walker (2015) have calculated the *P* derivatives for all the C_{ij}s of omphacite at 0 K. According to their results, C_{15}, C_{25}, C_{35}, and C_{46} have negative *P* derivatives, which are in agreement with the experimental measurements of diopside (Sang & Bass, 2014). In this study, dC_{25}/dP is slightly positive and dC_{15}/dP is close to 0. Compared with previous studies, Skelton and Walker (2015) calculated the high-*P* elastic properties at 0 K which is different from 300 K in this study. Sang and Bass (2014)

Table 1
Single-Crystal and Aggregate Elastic Properties of Omphacite at Different Pressures Determined in This Study

Pressure	1 atm	3.0 (1) GPa	6.0 (1) GPa	8.9 (1) GPa	12.0 (1) GPa	15.0 (1) GPa	18.0 (1) GPa
ρ (g/cm^3)	3.340	3.419	3.492	3.558	3.625	3.686	3.744
C_{11} (GPa)	231.5 (8)	259 (1)	277.2 (8)	294.3 (7)	315.3 (8)	333.2 (7)	348.6 (6)
C_{22} (GPa)	201 (1)	213 (2)	229 (1)	247 (1)	262 (1)	277 (1)	289 (1)
C_{33} (GPa)	253.8 (8)	275 (1)	297.6 (8)	314.2 (7)	326.3 (8)	346.8 (8)	356.7 (6)
C_{44} (GPa)	79.1 (5)	82.3 (6)	86.0 (6)	87.6 (5)	91.0 (6)	92.5 (6)	97.7 (6)
C_{55} (GPa)	68.9 (4)	70.7 (5)	74.0 (5)	78.4 (4)	81.9 (4)	84.5 (4)	88.1 (3)
C_{66} (GPa)	74.0 (4)	80.3 (7)	89.7 (5)	95.7 (6)	101.4 (5)	109.6 (5)	119.1 (5)
C_{12} (GPa)	84.4 (9)	96 (1)	107.6 (8)	120.7 (8)	131.6 (9)	144.5 (9)	146.7 (9)
C_{13} (GPa)	76 (1)	85 (1)	93 (1)	104.2 (9)	118 (1)	122 (1)	132.6 (8)
C_{23} (GPa)	60 (2)	71 (2)	77 (2)	89 (2)	89 (2)	99 (2)	120 (2)
C_{15} (GPa)	7.6 (5)	5.6 (6)	5.6 (5)	4.4 (4)	4.6 (5)	6.3 (5)	6.5 (4)
C_{25} (GPa)	5.4 (10)	4 (1)	5.9 (9)	6 (1)	10 (1)	11 (1)	22 (1)
C_{35} (GPa)	39.8 (5)	33.2 (6)	28.5 (5)	26.4 (4)	23.8 (5)	21.5 (5)	23.2 (4)
C_{46} (GPa)	5.9 (4)	6.4 (6)	7.0 (5)	7.2 (6)	6.5 (6)	2.2 (6)	−1.8 (5)
K_S^R (GPa)	119.9 (5)	134.7 (6)	146.7 (6)	161.3 (5)	171.3 (6)	183.4 (6)	193.6 (5)
G^R (GPa)	71.9 (2)	76.7 (3)	82.2 (3)	85.8 (3)	90.0 (3)	94.0 (3)	97.8 (2)
K_S^V (GPa)	125.3 (5)	138.8 (6)	150.8 (6)	164.8 (5)	175.8 (6)	187.6 (6)	199.2 (5)
G^V (GPa)	75.4 (2)	79.7 (3)	85.0 (3)	88.4 (3)	92.5 (3)	96.7 (3)	100.7 (2)
K_S^{VRH} (GPa)	123 (3)	137 (3)	149 (2)	163 (2)	174 (3)	186 (3)	196 (3)
G^{VRH} (GPa)	74 (2)	78 (2)	84 (2)	87 (2)	91 (2)	95 (2)	99 (2)
Vp (km/s)	8.13 (4)	8.40 (3)	8.63 (3)	8.86 (2)	9.02 (3)	9.21 (3)	9.37 (3)
Vs (km/s)	4.70 (3)	4.78 (3)	4.89 (3)	4.95 (2)	5.02 (2)	5.09 (2)	5.15 (2)

Note. VRH = Voigt-Reuss-Hill.

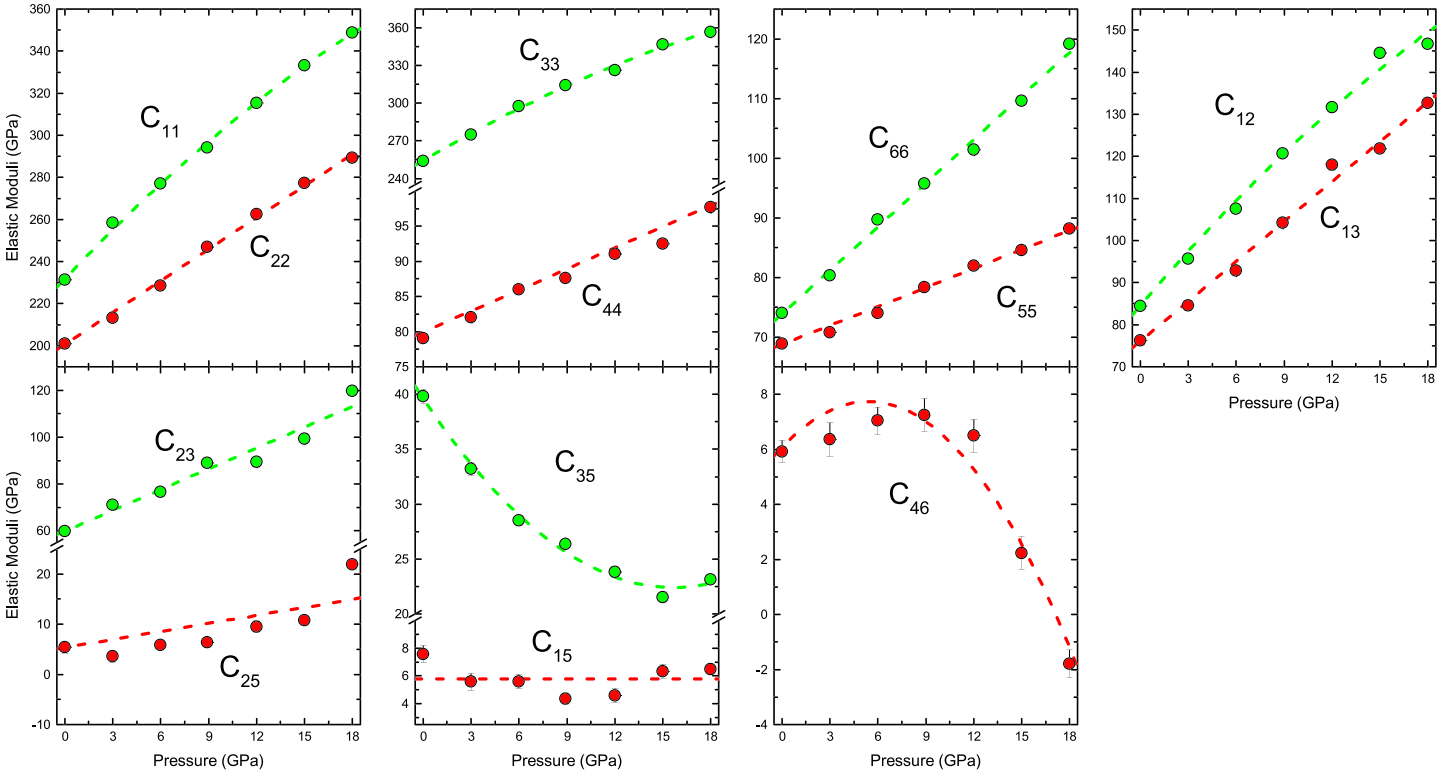

Figure 4. Single-crystal elastic moduli of omphacite at high-*P* conditions. The dashed lines represent the best fit finite strain elastic models.

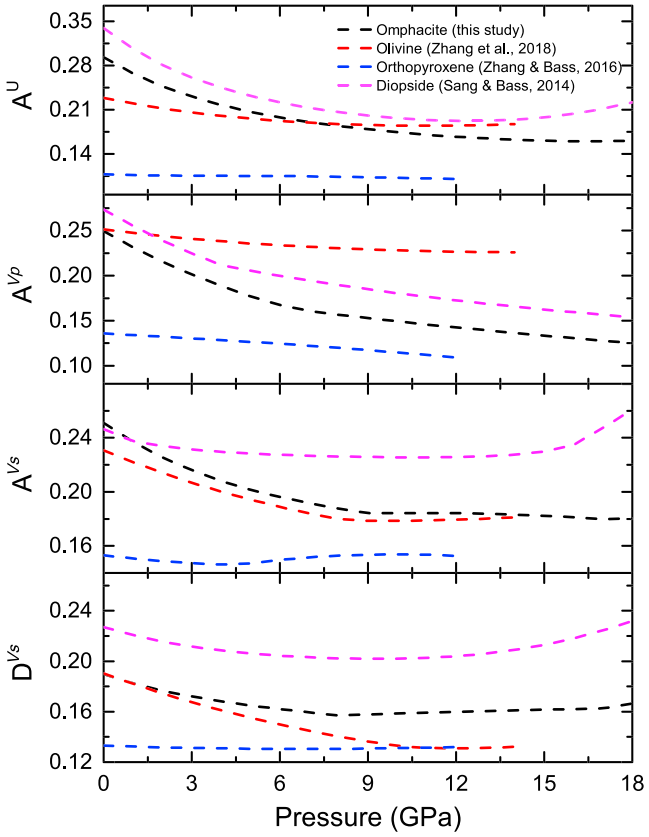

Figure 5. The anisotropy indices (A^{U}, A^{Vp}, A^{Vs}, and D^{Vs}) of omphacite, olivine (J. S. Zhang et al., 2018), and orthopyroxene (J. S. Zhang & Bass, 2016).

performed the measurements for pure diopside end member, whereas the omphacite crystals used in this study have ~29.5% jadeite component. The *T* and compositional difference might cause the deviation from these two previous studies.

3.3. Elastic Anisotropy of Omphacite at High-*P* Conditions

Omphacite, garnet, and high-*P* silica phase are the major constituents of eclogite. Omphacite is the major anisotropy contributor due to the small volume percent of the silica phase and the elastically isotropic nature of the garnet. Thus, in order to study the anisotropic seismic properties of eclogite in the Earth's interior, it is important to understand the evolution of the elastic anisotropy of omphacite at high-*P* conditions.

In order to describe the elastic anisotropy of minerals, we have used four different anisotropy indices: Universal Anisotropy Index (A^{U}), the *Vp* and *Vs* azimuthal anisotropy A^{Vp} and A^{Vs}, and *Vs* polarization anisotropy D^{Vs}, which are defined in equations (S5)–(S8) in the supporting information. A^{U} is used as a measure of the overall elastic anisotropy for materials with arbitrary symmetry (Ranganathan & Ostoja-Starzewski, 2008). A^{Vp} or A^{Vs} represents the maximum velocity difference of all *Vp* or *Vs* propagating along different directions. D^{Vs} describes the maximum velocity difference between two orthogonally polarized shear waves propagating along the same direction.

Utilizing the obtained C_{ij}s for omphacite, we calculated all four anisotropy indices up to 18 GPa and also compared our obtained values with olivine, diopside, and orthopyroxene (Figure 5; J. S. Zhang et al., 2018; Sang & Bass, 2014; J. S. Zhang & Bass, 2016). For consistency, we adopted the same finite strain approach used in this study to reanalyze all the data presented in previous studies. The calculated *P* dependences of all the C_{ij}s for olivine, diopside, and orthopyroxene are shown in Table S4. Among all four different minerals, orthopyroxene has the lowest elastic anisotropy indices in its entire *P* stability field (J. S. Zhang et al., 2012). At ambient-*T* high-*P* conditions, diopside has the highest anisotropy of A^{U}, A^{Vs}, and D^{Vs}, whereas olivine has slightly higher A^{Vp} than diopside. At $P < \sim 12$ GPa, the elastic anisotropy of olivine, omphacite, and diopside all decrease with *P*. At $P > \sim 12$ GPa, the A^{U}, A^{Vs}, and D^{Vs} of diopside, as well as the D^{Vs} of omphacite, increase with *P*. This is in agreement with previous theoretical calculation results on omphacite and jadeite (Skelton & Walker, 2015; Walker, 2012). Within the investigated *P* range, omphacite has higher A^{Vs} and D^{Vs} yet lower A^{Vp} compared with olivine. Omphacite is a strong anisotropy contributor in the regions where eclogite lithology is expected.

3.4. Geophysical Implication

Recycled eclogitic, or basaltic component, is one of the most important chemical heterogeneities in the Earth's interior (Stixrude & Lithgow-Bertelloni, 2012; Xu et al., 2008). Due to the slow chemical diffusion and inefficient mixing, those chemical heterogeneities could be preserved through geological time (Ballmer et al., 2017). Locating the potentially eclogite-rich regions in the Earth's interior requires a better understanding of the seismic properties of eclogite (e.g., Ábalos et al., 2011). Utilizing the thermoelastic parameters of omphacite and other relevant minerals, we modeled the isotropic *Vp*, *Vs*, and the elastic anisotropy profiles of eclogite along mantle adiabats from 200- to 500-km depth (Katsura et al., 2010). Then we compared our results of eclogite with the ambient upper mantle model rock pyrolite. The thermoelastic parameters for the relevant mineral phases are listed in Table S5 (Arimoto et al., 2015; Chen et al., 2017; Fei, 1995; Gwanmesia et al., 2014; Irifune et al., 2008; Kulik et al., 2018; Li & Neuville, 2010; Liu et al., 2000; Reichmann et al., 2002; Sang & Bass, 2014; Sinogeikin & Bass, 2002; Suzuki & Anderson, 1983; Yang & Wu, 2014; J. S. Zhang et al., 2018; J. S. Zhang & Bass, 2016).

The aggregate velocities of eclogite are calculated based on the petrological models of Aoki and Takahashi (2004) from 200- to 500-km depth, and the velocities of pyrolite are adopted from Xu et al. (2008; Figure 6a).

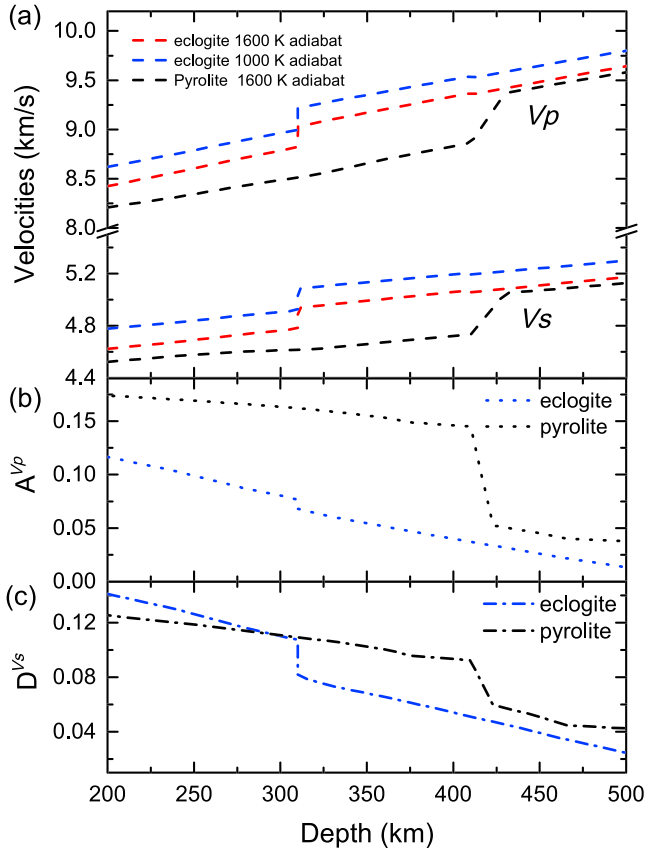

Figure 6. The (a) *Vp* and *Vs*, (c) D^{Vs}, and (b) A^{Vp} of pyrolite and eclogite in the Earth's interior.

It is worth noting that both the phase proportions and the chemical compositions of the minerals in eclogite change with depth. Previous studies have suggested different high-*P* petrological models of eclogite. Irifune et al. (1986) proposed that stishovite gradually exsoluted from the eclogite matrix, whereas Aoki and Takahashi (2004) and Xu et al. (2008) claimed that the coesite could be stabilized at depths <300 km. In the latter case, the coesite-stishovite transition can result in a velocity jump at ~310-km depth. Further studies are needed to clarify this issue.

The maximum A^{Vp} and D^{Vs} anisotropy of pyrolite and eclogite are estimated based on the proportions and *P*-dependent elastic anisotropy of different anisotropic minerals (Figure 6). We only considered the *P* effect due to the lack of the single-crystal elasticity measurements at high-*T* conditions. Finite strain approach was employed to reanalyze all previous data to ensure the consistency of the anisotropy comparison. Unfortunately, the C_{ij}s of coesite have not been experimentally determined at high-*P* conditions. Thus, a constant elastic anisotropy value was assumed within its stability field (Weidner & Carleton, 1977).

Between 200- and 500-km depths, the obtained isotropic velocities of eclogite are always higher than pyrolite along the 1600-K adiabat. The maximum *Vp* (~5.7%) and *Vs* (~7.1%) difference between the eclogite and pyrolite is at the depth range between 310 and 410 km, primarily due to the coesite-stishovite and olivine-wadsleyite transitions. The coesite-stishovite transition increases the *Vp* and *Vs* of eclogite by 2.3% and 3.3%, whereas the olivine-wadsleyite phase transition elevates the *Vp* and *Vs* of pyrolite by 5.1% and 6.2%, respectively. At depth >410 km, the velocities of pyrolite and eclogite are essentially identical (<0.9% difference), within the experimental uncertainty and seismic resolution. This result implies that, at least within the upper part of the transition zone, enrichment of eclogitic materials is unlikely to cause any compositional induced seismic anomalies. Considering eclogite is recycled back into the Earth's mantle through slab subduction, the *T* of eclogite can be several hundred kelvins lower than the ambient mantle (e.g., Syracuse et al., 2010). We thus calculated velocity profiles along a colder 1000-K adiabat (Figure 6a), and the *Vp* and *Vs* of eclogite are elevated by ~2.0% and 2.8%. In a realistic scenario, the maximum velocity difference of pyrolite and eclogite could be anywhere between 5.7% and 7.7% for *Vp* and between 7.1% and 9.9% for *Vs* between 310 and 410 km.

The maximum difference of A^{Vp} and D^{Vs} between pyrolite and eclogite is also observed between 310- and 410-km depths. At the 410 discontinuity, the olivine-wadsleyite transition decreases the A^{Vp} and D^{Vs} of pyrolite significantly due to the abrupt anisotropy drop across this phase transition (J. S. Zhang et al., 2018). At about 400 km, the A^{Vp} of pyrolite is ~3 times higher than eclogite. For the D^{Vs}, the trend is more interesting. At shallower depth eclogite has higher D^{Vs} than pyrolite because of the large proportion and high anisotropy of omphacite. This difference diminishes with depth due to the fast decrease of omphacite anisotropy as well as the dissolution of omphacite into the garnet structure. The coesite-stishovite transition takes place at ~310-km depth. Stishovite is less anisotropic than coesite at this depth. Thus, the D^{Vs} of eclogite drops from 10.7% to 8.1% at 310 km, and the D^{Vs} of pyrolite is ~75% higher than eclogite at 410 km.

The maximum isotropic and anisotropic velocities contrast between pyrolite and eclogite is at 310–410 km, making it an optimal depth range for seismologists to search for eclogite-rich heterogeneities in the Earth's interior. The ~5–7% velocity difference between eclogite and pyrolite also needs to be taken into account when estimating the slab temperatures between 310- and 410-km depths. Otherwise, the slab temperature could be underestimated by a few hundred kelvins without considering the possible lithology difference.

4. Conclusion

We have determined the thermal EOS and the single-crystal elastic properties of omphacite using synchrotron single-crystal XRD and Brillouin spectroscopy. The derived thermoelastic properties for omphacite are $K_{T0} = 118.7$ GPa, $K_{T0}' = 4.6$ (5), $\alpha_0 = 2.7$ (8) $\times 10^{-5}$ K^{-1}, $K_{S0} = 123$ (3) GPa, $G_0 = 74$ (2) GPa, $K_{S0}' = 4.5$ (3), and $G_0' = 1.6$ (1). Based on the modeled isotropic and anisotropic seismic properties of eclogite along different mantle adiabats, we found that the maximum isotropic and anisotropic velocity contrast between the eclogite and ambient pyrolitic mantle is at 310- to 410-km depth. Due to the ~5% to 7% higher velocities of eclogite compared with pyrolite between 310- and 410-km depth, the slab temperature estimation based on pure *T*-induced seismic velocity increase can be off without considering the existence of eclogitic lithology.

Acknowledgments
The authors would like to thank Jane Silverstone for providing the omphacite sample, Mike Spilde for the help with EPMA experiment at the Institute of Meteoritics at UNM, and Sergey Tkachev for the Neon gas loading of the DACs and the help with the room *P-T* XRD measurements for determining the crystal orientation at GSECARS. This work is supported by the National Science Foundation (NSF) under grant EAR 1646527 (J. Z.) and the start-up fund from UNM (J. Z.). The use of the gas-loading system, 13-BM-D, and 13-BM-C beamlines is supported by COMPRES, the Consortium for Materials Properties Research in Earth Sciences under NSF Cooperative Agreement EAR 1661511, and GSECARS funded by NSF (EAR-1634415), and Department of Energy (DOE)—GeoSciences (DE-FG02-94ER14466). This research used resources of the APS, a U.S. DOE Office of Science User Facility operated for the DOE Office of Science by Argonne National Laboratory under contract DE-AC02-06CH11357. The data presented in this study are available in the supporting information.

References

Ábalos, B., Fountain, D. M., Ibarguchi, J. G., & Puelles, P. (2011). Eclogite as a seismic marker in subduction channels: Seismic velocities, anisotropy, and petrofabric of Cabo Ortegal eclogite tectonites (Spain). *Bulletin*, *123*(3–4), 439–456. https://doi.org/10.1130/B30226.1

Ahrens, T. J., & Schubert, G. (1975). Gabbro-eclogite reaction rate and its geophysical significance. *Reviews of Geophysics*, *13*(2), 383–400. https://doi.org/10.1029/RG013i002p00383

Anderson, D. L. (2007). *New theory of the Earth*. New York: Cambridge University Press.

Anderson, O. L., Isaak, D. G., & Yamamoto, S. (1989). Anharmonicity and the equation of state for gold. *Journal of Applied Physics*, *65*(4), 1534–1543. https://doi.org/10.1063/1.342969

Angel, R. J., Alvaro, M., & Nestola, F. (2018). 40 years of mineral elasticity: A critical review and a new parameterisation of equations of state for mantle olivines and diamond inclusions. *Physics and Chemistry of Minerals*, *45*(2), 95–113. https://doi.org/10.1007/s00269-017-0900-7

Aoki, I., & Takahashi, E. (2004). Density of MORB eclogite in the upper mantle. *Physics of the Earth and Planetary Interiors*, *143*, 129–143. https://doi.org/10.1016/j.pepi.2003.10.007

Arimoto, T., Gréaux, S., Irifune, T., Zhou, C., & Higo, Y. (2015). Sound velocities of $Fe_3Al_2Si_3O_{12}$ almandine up to 19 GPa and 1700 K. *Physics of the Earth and Planetary Interiors*, *246*, 1–8. https://doi.org/10.1016/j.pepi.2015.06.004

Ballmer, M. D., Houser, C., Hernlund, J. W., Wentzcovitch, R. M., & Hirose, K. (2017). Persistence of strong silica-enriched domains in the Earth's lower mantle. *Nature Geoscience*, *10*(3), 236. https://doi.org/10.1038/ngeo2898

Bhagat, S. S., Bass, J. D., & Smyth, J. R. (1992). Single-crystal elastic properties of omphacite-C2/c by Brillouin spectroscopy. *Journal of Geophysical Research*, *97*(B5), 6843–6848. https://doi.org/10.1029/92JB00030

Birch, F. (1947). Finite elastic strain of cubic crystals. *Physical Review*, *71*(11), 809. https://doi.org/10.1103/PhysRev.71.809

Chen, T., Liebermann, R. C., Zou, Y., Li, Y., Qi, X., & Li, B. (2017). Tracking silica in Earth's upper mantle using new sound velocity data for coesite to 5.8 GPa and 1073 K. *Geophysical Research Letters*, *44*, 7757–7765. https://doi.org/10.1002/2017GL073950

Clark, J. R., & Papike, J. J. (1968). Crystal-chemical characterization of omphacites. *American Mineralogist: Journal of Earth and Planetary Materials*, *53*(5–6), 840–868.

Davies, G. F. (1974). Effective elastic moduli under hydrostatic stress—I. Quasi-harmonic theory. *Journal of Physics and Chemistry of Solids*, *35*(11), 1513–1520. https://doi.org/10.1016/S0022-3697(74)80279-9

Davies, G. F., & Dziewonski, A. M. (1975). Homogeneity and constitution of the Earth's lower mantle and outer core. *Physics of the Earth and Planetary Interiors*, *10*(4), 336–343. https://doi.org/10.1016/0031-9201(75)90060-6

Dera, P., Zhuravlev, K., Prakapenka, V., Rivers, M. L., Finkelstein, G. J., Grubor-Urosevic, O., et al. (2013). High pressure single-crystal micro X-ray diffraction analysis with GSE_ADA/RSV software. *High Pressure Research*, *33*(3), 466–484. https://doi.org/10.1080/08957959.2013.806504

Dorogokupets, P. I., & Oganov, A. R. (2007). Ruby, metals, and MgO as alternative pressure scales: A semiempirical description of shock-wave, ultrasonic, x-ray, and thermochemical data at high temperatures and pressures. *Physical Review B*, *75*(2), 024115. https://doi.org/10.1103/PhysRevB.75.024115

Fei, Y. (1995). Thermal expansion. In *T. J. Ahrens mineral physics and crystallography: A handbook of physical constants* (Vol. 2, pp. 29–44). Washington, DC: American Geophysical Union.

Fei, Y., Ricolleau, A., Frank, M., Mibe, K., Shen, G., & Prakapenka, V. (2007). Toward an internally consistent pressure scale. *Proceedings of the National Academy of Sciences of the United States of America*, *104*(22), 9182–9186. https://doi.org/10.1073/pnas.0609013104

Fei, Y., van Orman, J., Li, J., van Westrenen, W., Sanloup, C., Minarik, W., et al. (2004). Experimentally determined postspinel transformation boundary in Mg_2SiO_4 using MgO as an internal pressure standard and its geophysical implications. *Journal of Geophysical Research*, *109*, B02305. https://doi.org/10.1029/2003JB002562

Fleet, M. E., Herzberg, C. T., Bancroft, G. M., & Aldridge, L. P. (1978). Omphacite studies; I, The P2/n--> C2/c transformation. *American Mineralogist*, *63*(11–12), 1100–1106.

Greeff, C. W., & Graf, M. J. (2004). Lattice dynamics and the high-pressure equation of state of Au. *Physical Review B*, *69*(5), 054,107. https://doi.org/10.1103/PhysRevB.69.054107

Gwanmesia, G. D., Wang, L., Heady, A., & Liebermann, R. C. (2014). Elasticity and sound velocities of polycrystalline grossular garnet ($Ca_3Al_2Si_3O_{12}$) at simultaneous high pressures and high temperatures. *Physics of the Earth and Planetary Interiors*, *228*, 80–87. https://doi.org/10.1016/j.pepi.2013.09.010

Hill, R. (1963). Elastic properties of reinforced solids: Some theoretical principles. *Journal of the Mechanics and Physics of Solids*, *11*(5), 357–372. https://doi.org/10.1016/0022-5096(63)90036-X

Holland, T. J. B., & Powell, R. (2011). An improved and extended internally consistent thermodynamic dataset for phases of petrological interest, involving a new equation of state for solids. *Journal of Metamorphic Geology*, *29*(3), 333–383. https://doi.org/10.1111/j.1525-1314.2010.00923.x

Irifune, T., Higo, Y., Inoue, T., Kono, Y., Ohfuji, H., & Funakoshi, K. (2008). Sound velocities of majorite garnet and the composition of the mantle transition region. *Nature*, *451*(7180), 814. https://doi.org/10.1038/nature06551

Irifune, T., Sekine, T., Ringwood, A. E., & Hibberson, W. O. (1986). The eclogite-garnetite transformation at high pressure and some geophysical implications. *Earth and Planetary Science Letters*, *77*(2), 245–256. https://doi.org/10.1016/0012-821X(86)90165-2

Isaak, D. G., & Ohno, I. (2003). Elastic constants of chrome-diopside: Application of resonant ultrasound spectroscopy to monoclinic single-crystals. *Physics and Chemistry of Minerals*, *30*(7), 430–439. https://doi.org/10.1007/s00269-003-0334-2

Isaak, D. G., Ohno, I., & Lee, P. C. (2006). The elastic constants of monoclinic single-crystal chrome-diopside to 1,300 K. *Physics and Chemistry of Minerals*, *32*(10), 691–699. https://doi.org/10.1007/s00269-005-0047-9

Kandelin, J., & Weidner, D. J. (1988). The single-crystal elastic properties of jadeite. *Physics of the Earth and Planetary Interiors*, *50*(3), 251–260.

Kantor, I., Prakapenka, V., Kantor, A., Dera, P., Kurnosov, A., Sinogeikin, S., et al. (2012). BX90: A new diamond anvil cell design for X-ray diffraction and optical measurements. *Review of Scientific Instruments*, *83*(12), 125102. https://doi.org/10.1063/1.4768541

Katsura, T., Yoneda, A., Yamazaki, D., Yoshino, T., & Ito, E. (2010). Adiabatic temperature profile in the mantle. *Physics of the Earth and Planetary Interiors*, *183*(1–2), 212–218. https://doi.org/10.1016/j.pepi.2010.07.001

Kay, R. W., & Kay, S. M. (1993). Delamination and delamination magmatism. *Tectonophysics*, *219*(1–3), 177–189. https://doi.org/10.1016/0040-1951(93)90295-U

Kulik, E., Murzin, V., Kawaguchi, S., Nishiyama, N., & Katsura, T. (2018). Thermal expansion of coesite determined by synchrotron powder X-ray diffraction. *Physics and Chemistry of Minerals*, 1–9. https://doi.org/10.1007/s00269-018-0969-7

Levien, L., Weidner, D. J., & Prewitt, C. T. (1979). Elasticity of diopside. *Physics and Chemistry of Minerals*, *4*(2), 105–113. https://doi.org/10.1007/BF00307555

Li, B., & Neuville, D. R. (2010). Elasticity of diopside to 8 GPa and 1073 K and implications for the upper mantle. *Physics of the Earth and Planetary Interiors*, *183*(3–4), 398–403. https://doi.org/10.1016/j.pepi.2010.08.009

Liu, J., Chen, G., Gwanmesia, G. D., & Liebermann, R. C. (2000). Elastic wave velocities of pyrope–majorite garnets ($Py_{62}Mj_{38}$ and $Py_{50}Mj_{50}$) to 9 GPa. *Physics of the Earth and Planetary Interiors*, *120*(1–2), 153–163. https://doi.org/10.1016/S0031-9201(00)00152-7

Mao, H. K., Bell, P. M., Shaner, J. T., & Steinberg, D. J. (1978). Specific volume measurements of Cu, Mo, Pd, and Ag and calibration of the ruby R 1 fluorescence pressure gauge from 0.06 to 1 Mbar. *Journal of Applied Physics*, *49*(6), 3276–3283. https://doi.org/10.1063/1.325277

Matsui, M., & Busing, W. R. (1984). Calculation of the elastic constants and high-pressure properties of diopside, $CaMgSi_2O_6$. *American Mineralogist*, *69*, 1090–1095.

Mauler, A., Burlini, L., Kunze, K., Philippot, P., & Burg, J. P. (2000). *P*-wave anisotropy in eclogites and relationship to the omphacite crystallographic fabric. *Physics and Chemistry of the Earth, Part A: Solid Earth and Geodesy*, *25*(2), 119–126. https://doi.org/10.1016/S1464-1895(00)00020-X

McCormick, T. C., Hazen, R. M., & Angel, R. J. (1989). Compressibility of omphacite to 60 kbar; Role of vacancies. *American Mineralogist*, *74*(11–12), 1287–1292.

Moghadam, R. H., Trepmann, C. A., Stöckhert, B., & Renner, J. (2010). Rheology of synthetic omphacite aggregates at high pressure and high temperature. *Journal of Petrology*, *51*(4), 921–945. https://doi.org/10.1093/petrology/egq006

Nishihara, Y., Takahashi, E., Matsukage, K., & Kikegawa, T. (2003). Thermal equation of state of omphacite. *American Mineralogist*, *88*(1), 80–86. https://doi.org/10.2138/am-2003-0110

Pandolfo, F., Cámara, F., Domeneghetti, M. C., Alvaro, M., Nestola, F., Karato, S. I., & Amulele, G. (2015). Volume thermal expansion along the jadeite–diopside join. *Physics and Chemistry of Minerals*, *42*(1), 1–14. https://doi.org/10.1007/s00269-014-0694-9

Pandolfo, F., Nestola, F., Cámara, F., & Domeneghetti, M. C. (2012a). High-pressure behavior of space group P2/n omphacite. *American Mineralogist*, *97*(2–3), 407–414. https://doi.org/10.2138/am.2012.3928

Pandolfo, F., Nestola, F., Cámara, F., & Domeneghetti, M. C. (2012b). New thermoelastic parameters of natural C2/c omphacite. *Physics and Chemistry of Minerals*, *39*(4), 295–304. https://doi.org/10.1007/s00269-012-0484-1

Pavese, A., Bocchio, R., & Ivaldi, G. (2000). In situ high temperature single crystal X-ray diffraction study of a natural omphacite. *Mineralogical Magazine*, *64*(6), 983–993. https://doi.org/10.1180/002646100549986

Pavese, A., Diella, V., Levy, D., & Hanfland, M. (2001). Synchrotron X-ray powder diffraction study of natural P2/n-omphacites at high-pressure conditions. *Physics and Chemistry of Minerals*, *28*(1), 9–16. https://doi.org/10.1007/s002690000128

Peacock, S. M. (1996). Thermal and petrologic structure of subduction zones. In *Subduction: Top to bottomGeophysical Monograph Series* (Vol. 96, pp. 119–133). Washington, DC: American Geophysical Union. https://doi.org/10.1029/GM096p0119

Ranganathan, S. I., & Ostoja-Starzewski, M. (2008). Universal elastic anisotropy index. *Physical Review Letters*, *101*(5), 055,504. https://doi.org/10.1103/PhysRevLett.101.055504

Reichmann, H. J., Sinogeikin, S. V., Bass, J. D., & Gasparik, T. (2002). Elastic moduli of jadeite-enstatite majorite. *Geophysical Research Letters*, *29*(19), 1936. https://doi.org/10.1029/2002GL015106

Rivers, M., Prakapenka, V. B., Kubo, A., Pullins, C., Holl, C. M., & Jacobsen, S. D. (2008). The COMPRES/GSECARS gas-loading system for diamond anvil cells at the advanced photon source. *High Pressure Research*, *28*(3), 273–292. https://doi.org/10.1080/08957950802333593

Sang, L., & Bass, J. D. (2014). Single-crystal elasticity of diopside to 14 GPa by Brillouin scattering. *Physics of the Earth and Planetary Interiors*, *228*, 75–79. https://doi.org/10.1016/j.pepi.2013.12.011

Sang, L., Vanpeteghem, C. B., Sinogeikin, S. V., & Bass, J. D. (2011). The elastic properties of diopside, CaMgSi2O6. *American Mineralogist*, *96*(1), 224–227. https://doi.org/10.2138/am.2011.3674

Shim, S. H., Duffy, T. S., & Takemura, K. (2002). Equation of state of gold and its application to the phase boundaries near 660 km depth in Earth's mantle. *Earth and Planetary Science Letters*, *203*(2), 729–739. https://doi.org/10.1016/S0012-821X(02)00917-2

Sinogeikin, S. V., & Bass, J. D. (2002). Elasticity of majorite and a majorite-pyrope solid solution to high pressure: Implications for the transition zone. *Geophysical Research Letters*, *29*(2), 1017. https://doi.org/10.1029/2001GL013937

Skelton, R., & Walker, A. M. (2015). The effect of cation order on the elasticity of omphacite from atomistic calculations. *Physics and Chemistry of Minerals*, *42*(8), 677–691. https://doi.org/10.1007/s00269-015-0754-9

Stixrude, L., & Lithgow-Bertelloni, C. (2012). Geophysics of chemical heterogeneity in the mantle. *Annual Review of Earth and Planetary Sciences*, *40*, 569–595. https://doi.org/10.1146/annurev.earth.36.031207.124244

Suzuki, I., & Anderson, O. L. (1983). Elasticity and thermal expansion of a natural garnet up to 1,000 K. *Journal of Physics of the Earth*, *31*(2), 125–138. https://doi.org/10.4294/jpe1952.31.125

Syracuse, E. M., van Keken, P. E., & Abers, G. A. (2010). The global range of subduction zone thermal models. *Physics of the Earth and Planetary Interiors*, *183*(1–2), 73–90. https://doi.org/10.1016/j.pepi.2010.02.004

Tsuchiya, T. (2003). First-principles prediction of the *P-V-T* equation of state of gold and the 660-km discontinuity in Earth's mantle. *Journal of Geophysical Research*, *108*(B10), 2462. https://doi.org/10.1029/2003JB002446

Walker, A. M. (2012). The effect of pressure on the elastic properties and seismic anisotropy of diopside and jadeite from atomic scale simulation. *Physics of the Earth and Planetary Interiors*, *192*, 81–89. https://doi.org/10.1016/j.pepi.2011.10.002

Weidner, D. J., & Carleton, H. R. (1977). Elasticity of coesite. *Journal of Geophysical Research*, *82*(8), 1334–1346. https://doi.org/10.1029/JB082i008p01334

Xu, W., Lithgow-Bertelloni, C., Stixrude, L., & Ritsema, J. (2008). The effect of bulk composition and temperature on mantle seismic structure. *Earth and Planetary Science Letters*, *275*(1–2), 70–79. https://doi.org/10.1016/j.epsl.2008.08.012

Yang, R., & Wu, Z. (2014). Elastic properties of stishovite and the $CaCl_2$-type silica at the mantle temperature and pressure: An ab initio investigation. *Earth and Planetary Science Letters*, *404*, 14–21. https://doi.org/10.1016/j.epsl.2014.07.020

Zhang, D., Dera, P. K., Eng, P. J., Stubbs, J. E., Zhang, J. S., Prakapenka, V. B., & Rivers, M. L. (2017). High pressure single crystal diffraction at PX^2. *Journal of Visualized Experiments*, *119*, 54660. https://doi.org/10.3791/54660

Zhang, D., Hu, Y., & Dera, P. K. (2016). Compressional behavior of omphacite to 47 GPa. *Physics and Chemistry of Minerals*, *43*(10), 707–715. https://doi.org/10.1007/s00269-016-0827-4

Zhang, J., & Green, H. W. (2007). Experimental investigation of eclogite rheology and its fabrics at high temperature and pressure. *Journal of Metamorphic Geology*, *25*(2), 97–115. https://doi.org/10.1111/j.1525-1314.2006.00684.x

Zhang, J., Green, H. W. II, & Bozhilov, K. N. (2006). Rheology of omphacite at high temperature and pressure and significance of its lattice preferred orientations. *Earth and Planetary Science Letters*, *246*(3–4), 432–443. https://doi.org/10.1016/j.epsl.2006.04.006

Zhang, J. S., & Bass, J. D. (2016). Single-crystal elasticity of natural Fe-bearing orthoenstatite across a high-pressure phase transition. *Geophysical Research Letters*, *43*, 8473–8481. https://doi.org/10.1002/2016GL069963

Zhang, J. S., Bass, J. D., & Schmandt, B. (2018). The elastic anisotropy change near the 410-km discontinuity: Predictions from single-crystal elasticity measurements of olivine and wadsleyite. *Journal of Geophysical Research: Solid Earth*, *123*, 2674–2684. https://doi.org/10.1002/2017JB015339

Zhang, J. S., Bass, J. D., Taniguchi, T., Goncharov, A. F., Chang, Y. Y., & Jacobsen, S. D. (2011). Elasticity of cubic boron nitride under ambient conditions. *Journal of Applied Physics*, *109*(6), 063521. https://doi.org/10.1063/1.3561496

Zhang, J. S., Bass, J. D., & Zhu, G. (2015). Single-crystal Brillouin spectroscopy with CO_2 laser heating and variable q. *Review of Scientific Instruments*, *86*(6), 063905. https://doi.org/10.1063/1.4922634

Zhang, J. S., Dera, P., & Bass, J. D. (2012). A new high-pressure phase transition in natural Fe-bearing orthoenstatite. *American Mineralogist*, *97*(7), 1070–1074. https://doi.org/10.2138/am.2012.4072